Journal of Materials Chemistry A

ROYAL SOCIETY OF CHEMISTRY

PAPER

View Article Online
View Journal

Cite this: DOI: 10.1039/d6ta03240k

$NiCoO_x$@NiCo core–shell nanoparticles supported on $Ti_3C_2T_x$ as cathode electrocatalyst for microbial fuel cells

Pewee D. Kolubah, [a] Hend Omar Mohamed,*[a] Mohamed Nejib Hedhili, [b] Mohamed Ben Hassine,[b] Rafia Ahmad,[c] Vijay K. Velisoju,[a] Abdul-Hamid Emwas,[b] Pia Dally,[a] Luigi Cavallo [c] and Pedro Castaño *[ad]

The intrinsically sluggish oxygen reduction reaction (ORR) at platinum-group-metal-free cathodes remains a key bottleneck for the practical deployment of microbial fuel cells (MFCs). $Ti_3C_2T_x$ MXene is a promising conductive scaffold, yet its ORR activity is hindered by strong O_2 adsorption at Ti sites, leading to sluggish kinetics at neutral pH. Here, we address this limitation by developing a targeted chemical-reduction strategy that assembles NiCo alloy nanocores encapsulated in a thin NiCo-oxide shell (~4 nm) onto $Ti_3C_2T_x$, forming a ($NiCoO_x$@NiCo)/$Ti_3C_2T_x$ heterostructure catalyst. The core–shell domains modulate the local electronic environment, lower the O_2 binding energy, and introduce abundant active sites, thereby leveraging the high conductivity of $Ti_3C_2T_x$. As an air-cathode MFC treating glucose-supplemented wastewater, the catalyst delivers a current density of 4.5 A m^{-2} and a peak power density of 1.6 W m^{-2}, outperforming pristine $Ti_3C_2T_x$. This work establishes a generalizable heterostructure design strategy for activating MXene-based catalysts toward efficient neutral-pH ORR, bridging fundamental catalyst design with practical microbial fuel cell applications.

Received 17th April 2026
Accepted 31st May 2026

DOI: 10.1039/d6ta03240k

rsc.li/materials-a

1. Introduction

The oxygen reduction reaction (ORR) is a cornerstone process in electrochemical energy conversion technologies, yet its intrinsically sluggish kinetics often limit overall efficiency and durability.[1] Achieving high ORR performance requires catalysts that simultaneously provide abundant accessible active sites, optimized electronic structures, and long-term stability under operating conditions.[2] These characteristics are especially vital for electrochemical energy technologies, such as electrolyzers,[3,4] microbial fuel cells (MFCs), enzymatic, and hydrogen fuel cells,[5–7] and rechargeable batteries,[8] where efficient oxygen electrochemistry under mild or neutral conditions remains a significant challenge.

Among these technologies, MFCs have attracted increasing attention as a promising platform for simultaneous wastewater treatment and electricity generation.[9] However, their large-scale implementation is constrained by the performance and cost of cathode catalysts.[10–12] Platinum-based materials remain the benchmark for ORR, but their high cost, scarcity, and susceptibility to deactivation limit practical deployment. Notably, the cathode alone accounts for nearly half of the total system cost, underscoring the urgent need for efficient and durable platinum-group-metal-free alternatives.[13,14] Despite extensive progress in acidic and alkaline systems, the development of high-performance ORR catalysts under neutral conditions relevant to MFCs remains comparatively underexplored.

Two-dimensional (2D) materials have emerged as promising candidates for electrocatalysis due to their high surface area and tunable electronic properties.[15] However, conventional 2D systems present intrinsic limitations. For example, graphene exhibits excellent conductivity but lacks intrinsic catalytic activity, requiring defect engineering or heteroatom doping to introduce active sites.[16] Transition metal dichalcogenides (TMDs), such as MoS_2, display catalytic activity primarily at edge sites, while their basal planes remain largely inert, and their semiconducting nature restricts charge transfer.[17] Similarly, layered double hydroxides (LDHs) and related materials often suffer from low electrical conductivity, limiting their performance in electron-transfer-driven reactions.[18]

MXenes, particularly $Ti_3C_2T_x$, have emerged as a distinctive class of 2D materials that combine metallic conductivity, hydrophilic surfaces, and tunable surface terminations. These properties enable efficient charge transport and provide opportunities to modulate the adsorption energetics of reaction

[a]Multiscale Reaction Engineering, KAUST Catalysis Center (KCC), King Abdullah University of Science and Technology (KAUST), Thuwal, 23955-6900, Saudi Arabia. E-mail: hend.mohamed@kaust.edu.sa; pedro.castano@kaust.edu.sa

[b]Core Labs, King Abdullah University of Science and Technology (KAUST), Thuwal, 23955-6900, Saudi Arabia

[c]KAUST Catalysis Center (KCC), King Abdullah University of Science and Technology (KAUST), Thuwal, 23955-6900, Saudi Arabia

[d]Chemical Engineering Program, Physical Science and Engineering (PSE) Division, King Abdullah University of Science and Technology, Saudi Arabia

intermediates. Unlike many 2D systems, $Ti_3C_2T_x$ exhibits intrinsically accessible basal planes, making it a promising platform for electrocatalysis. However, its ORR activity remains limited due to excessively strong adsorption of oxygen intermediates (*O and *OH) at Ti sites, which impedes reaction turnover, particularly under neutral-pH conditions.[19] Therefore, strategies that can precisely tune the electronic structure and intermediate binding energies are essential to unlock its catalytic potential.[19,20]

Heterostructure engineering offers an effective route to address this limitation. Incorporating transition-metal alloys onto $Ti_3C_2T_x$ can induce interfacial electronic coupling, modify the d-band structure, and optimize adsorption energetics, thereby enhancing catalytic activity.[21] Density functional theory (DFT) studies have demonstrated that dual-metal systems, such as Ni–Co, can synergistically regulate the adsorption of ORR intermediates and lower the activation barriers. However, experimental validation of these concepts under neutral-pH conditions relevant to MFCs remains limited.[22,23]

In parallel, core–shell architectures combining metallic alloys and oxides have shown promise in oxygen electrocatalysis.[24,25] In these systems, the metallic core provides high electrical conductivity and efficient charge transport, while the oxide shell offers abundant redox-active sites and favorable adsorption properties.[24] The interplay between these components can create highly active and stable catalytic interfaces.[25] Nevertheless, most studies have focused on alkaline or acidic environments, and their applicability to neutral-pH MFC systems remains largely unexplored.

In this work, we address these challenges by designing a ($NiCoO_x$@NiCo)/$Ti_3C_2T_x$ heterostructure catalyst, in which NiCo alloy nanocores encapsulated within a thin oxide shell are integrated with conductive $Ti_3C_2T_x$ sheets. This design is intended to modulate the local electronic structure, optimize the adsorption energetics of oxygen intermediates, and facilitate charge transfer under neutral conditions. By combining MXene surface chemistry with alloy-oxide core–shell engineering and interfacial electronic coupling, this approach provides a platform to overcome the intrinsic limitations of $Ti_3C_2T_x$. More broadly, it offers a rational framework for developing efficient and durable platinum-group-metal-free ORR catalysts tailored for neutral-pH electrochemical systems such as microbial fuel cells.

2. Experimental

2.1. Catalyst synthesis

2.1.1. Synthesis of $Ti_3C_2T_x$ MXene. The $Ti_3C_2T_x$ MXene was synthesized from Ti_3AlC_2 MAX phase following a modified etching delamination procedure.[26] Briefly, 1 g of the Ti_3AlC_2 MAX powder (99.99%, Carbon Ukraine) was gradually added (0.2 g min^{-1}) to a mixed etchant containing hydrofluoric acid (HF, 40 wt%, Sung Young Chemical Limited), hydrochloric acid (HCl, 37%, VWR Chemicals), and deionized (DI) water in a volume ratio of 1 : 6 : 3 (total volume:10 mL). The mixture was stirred continuously at 45 °C for 16 h.

The obtained suspension was washed repeatedly with DI water (45 mL DI per wash; 3500 rpm; 5 min per cycle) until a stable dispersion was obtained. The washed product was then intercalated using 0.5 M lithium chloride (LiCl, 99%, Sigma-Aldrich) and subsequently delaminated *via* centrifugation to yield few-layer $Ti_3C_2T_x$ sheets. The resulting colloidal suspension was stored under an argon atmosphere at 4 °C for further use.

2.1.2. Synthesis of $NiCoO_x$@NiCo. The $NiCoO_x$@NiCo catalyst was synthesized *via* a combined chemical reduction and thermal treatment approach.[9] First, equimolar quantities of nickel(II) chloride hexahydrate ($NiCl_2 \cdot 6H_2O$; 0.2025 g) and cobalt(II) chloride dihydrate ($CoCl_2 \cdot 2H_2O$; 0.1407 g) were separately dissolved in 10 mL of DI water. The Ni precursor was then added dropwise to the Co precursor solution under continuous stirring, followed by further mixing for 10 min (320 rpm). Separately, 0.5 g of polyvinylpyrrolidone (PVP, $(C_6H_9NO)_n$, MW 10000, Thermo Fisher Scientific) was dissolved in 20 mL of DI water, and the solution was gradually added to the above mixture, which was maintained at 55 °C with continuous stirring for 30 min. Subsequently, 0.4 mM sodium borohydride ($NaBH_4$, 98%, Thermo Fisher Scientific) was added dropwise to initiate reduction, and the reaction was allowed to proceed for 60 min. The resulting precipitate was collected, washed 6 times with DI water and ethanol to remove residual reagents, and then vacuum-dried at 70 °C overnight. The dried product was thermally reduced at 400 °C (heating rate: 5 °C min^{-1}) for 2 h under a 5% H_2/Ar flow (100 mL min^{-1}).

2.1.3. Synthesis of ($NiCoO_x$@NiCo)/$Ti_3C_2T_x$ composite. To prepare the composite catalyst, 50 mg of $NiCoO_x$@NiCo was dispersed in 10 mL of $Ti_3C_2T_x$ colloidal suspension under continuous mixing. The mixture was dried at 70 °C under an argon atmosphere, followed by mild thermal treatment at 150 °C for 1 h under a 5% H_2/Ar flow to promote interfacial integration between $NiCoO_x$@NiCo and $Ti_3C_2T_x$. A schematic illustration of the synthesis procedure is presented in Fig. 1.

2.2. Catalyst characterization

Powder X-ray diffraction (XRD) patterns of the synthesized catalysts were recorded using a Bruker D8 Advance diffractometer operating at 40 kV and 40 mA with Cu Kα radiation (λ = 1.5406 Å), over a 2θ range of 5–90° with a step size of 0.05°, and the resulting patterns were analyzed using DIFFRAC.EVA software. The lattice strain induced by combining $Ti_3C_2T_x$ and $NiCoO_x$@NiCo was estimated by first computing the d spacing from the (111) plane of $NiCoO_x$@NiCo, using Bragg's law. Next, the compressive lattice strain $\left(\varepsilon = \frac{d - d_0}{d_0}\right)$ was evaluated based on the previously reported relative change in interplanar spacing.[27,28]

Quasi *in situ* X-ray photoelectron spectroscopy (XPS) measurements were performed using a Kratos Axis Supra spectrometer equipped with a monochromatic Al Kα source ($h\nu$ = 1486.6 eV). Measurements were conducted at 45 W under ultrahigh vacuum ($\sim 10^{-9}$ mbar). To minimize surface oxidation, samples were transferred under inert conditions from the

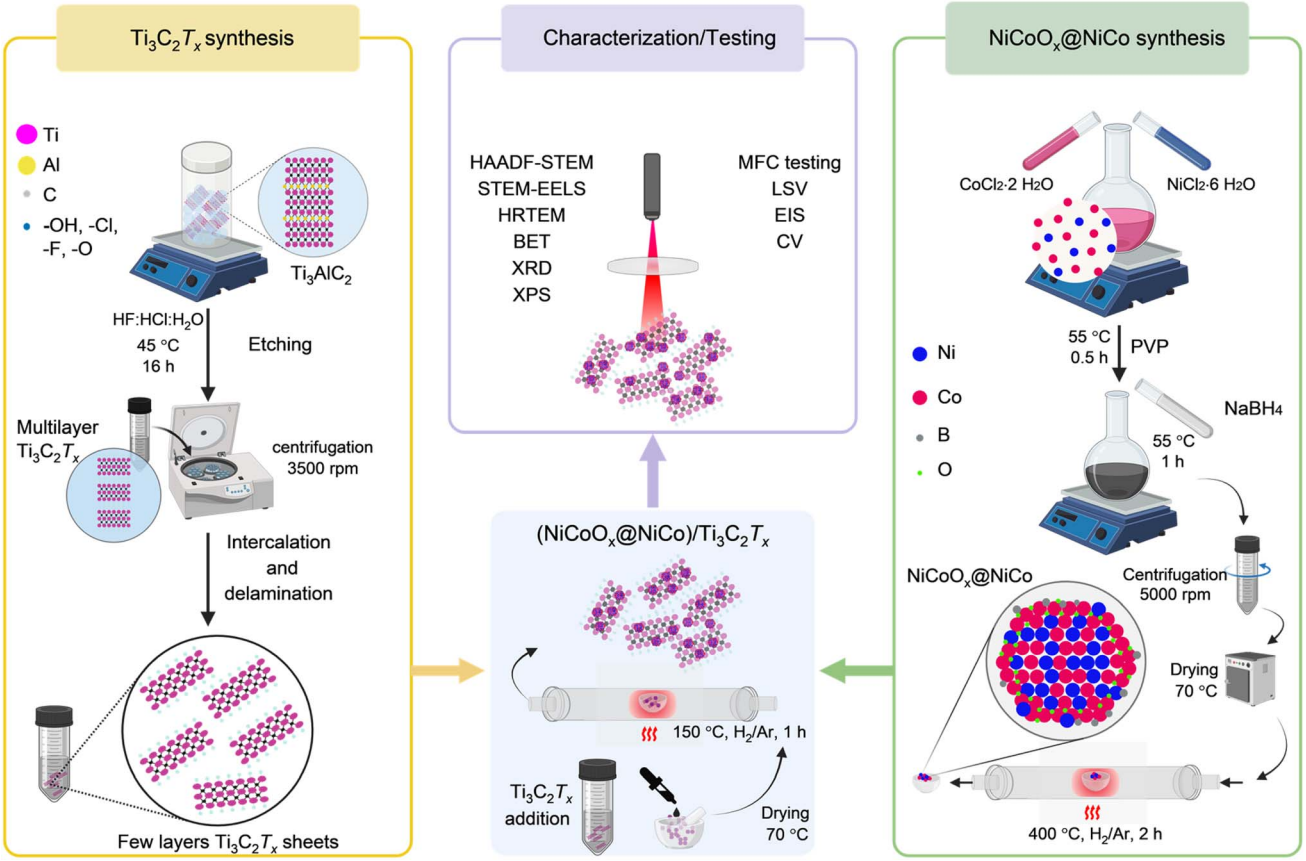

Fig. 1 Schematic overview of the synthesis procedures for $Ti_3C_2T_x$, $NiCoO_x$@NiCo, and the composite ($NiCoO_x$@NiCo)/$Ti_3C_2T_x$ catalyst, along with a summary of the physicochemical characterization techniques employed for catalyst evaluation.

reduction environment to a glovebox and mounted directly onto the XPS holder prior to analysis. Survey and high-resolution spectra were collected using pass energies of 80 eV and 20 eV, respectively, over an analysis area of 300 μm × 700 μm. Samples were mounted in floating mode to minimize differential charging effects during XPS measurements. Charge neutralization was applied for all samples. The binding energy scale was calibrated using the main Ni $2p_{3/2}$ peak corresponding to metallic Ni^0, which was referenced at 852.6 eV. The peak deconvolution was carried out following the semi-empirical fitting approach reported.[29] where the fitting procedure was applied to quantify the photoelectron contributions corresponding to the different chemical states present in the spectra.

Inductively coupled plasma optical emission spectroscopy (ICP-OES) was performed using Varian, Inc./Agilent Model 7200-ES, to quantify the elemental composition of the catalysts. For microwave-assisted digestion, approximately 0.03 g of catalyst was added to a mixture of concentrated HCl (1 mL), concentrated HNO_3 (3 mL), and concentrated HF (1 mL). The mixture was then digested under microwave irradiation with a 15 min ramp, and a 30 min hold at 493 K and 1000 W.

The Electron Paramagnetic Resonance (EPR) spectroscopy was conducted using a Bruker ELEXSYS E500 EPR spectrometer operating in the X-band region, equipped with a high-sensitivity ER 4122 SHQ resonator. Measurements were performed at ambient temperature with a microwave frequency of 9.3964 GHz and a sweep width of 8000 G. Field modulation was applied at 100 kHz with a modulation amplitude of 5 G. The microwave power was set to 0.0474 W. Data acquisition and processing were carried out using Bruker Xenon software.

High-resolution transmission electron microscopy (HR-TEM), high-angle annular dark-field scanning transmission electron microscopy (HAADF-STEM), and electron energy-loss spectroscopy (EELS) were employed to investigate catalyst morphology and elemental distribution. STEM imaging was performed using a Thermo Fisher Scientific Titan Themis Z microscope equipped with an HAADF detector, operating at 300 kV and 0.05 nA. HAADF-STEM images were obtained at a convergence angle of 20.9 mrad.

The nitrogen adsorption–desorption isotherms were measured at 77 K using a Micromeritics ASAP 2050 analyzer to assess the surface characteristics of the catalyst samples. Specific surface area was determined using the Brunauer–Emmett–Teller (BET) method. Scanning electron microscopy (SEM) was used to examine biofilm attachment on the MFC anode. Imaging was performed using a Thermo Fisher Scientific Quattro microscope.

2.3. Electrochemical testing

The electrocatalytic performance was evaluated using a standard three-electrode configuration on a CH instruments

workstation equipped with a rotating disk electrode (RDE). A catalyst-coated glassy carbon disk (3 mm diameter) served as the working electrode, with a graphite rod as the counter electrode. Reference electrodes were selected according to the electrolyte: Ag/AgCl for ORR measurements in phosphate-buffered saline (PBS, pH 7.4) and Hg/HgO for OER measurements in 0.5 M KOH (pH 13.2).

Prior to ORR measurements, the electrolyte was purged with N_2 for 30 min to remove dissolved oxygen, followed by bubbling with O_2 for 1 h to achieve saturation. For OER testing, the electrolyte was purged with N_2 for 30 min. Catalyst inks were prepared by dispersing 5 mg of (NiCoO_x@NiCo)/$Ti_3C_2T_x$ powder in a mixture of 960 μL isopropanol, 10 μL deionized water, and 30 μL Nafion solution, followed by sonication for 1 h. The ink was drop-cast onto the glassy carbon electrode (loading: 0.42 mg cm^{-2}) and dried under ambient conditions. Linear sweep voltammetry (LSV) was conducted at scan rates of 10 mV s^{-1} (ORR) and 1 mV s^{-1} (OER) with a rotation speed of 1600 rpm. All potentials were converted to the reversible hydrogen electrode (RHE) scale using the Nernst equation. Cyclic voltammetry (CV) measurements were performed under identical electrolyte conditions.

2.4. Microbial fuel cell testing

The ORR activity of the catalyst was evaluated in a single-chamber MFC equipped with an air-cathode and a total anodic volume of 100 mL (80 mL electrolyte and 20 mL headspace). A Nafion™ 117 membrane (NARA Cell-Tech Corporation, South Korea) separated the anode and cathode compartments to facilitate proton transport while minimizing oxygen crossover. The carbon paper (CP) and carbon cloth (CC) were pretreated by ultrasonication in acetone, rinsed with deionized water, and dried at 70 °C overnight. The cathode was prepared by depositing the catalyst onto CP (2.4 × 2.4 cm^2), while pretreated CC served as the anode. Both electrodes were connected to stainless-steel current collectors.

The anolyte was prepared from domestic wastewater collected from the KAUST treatment facility, supplemented with 20 mL of 1 M glucose to increase the organic content and stimulate microbial activity. The MFC was operated under ambient conditions, and cell voltage was continuously monitored. Polarization curves were obtained using linear sweep voltammetry (1 mV s^{-1}) after stabilization under open-circuit conditions. The internal resistance was determined from the slope of the linear region of the polarization curve.[30]

2.5. Electrochemical calculations

The electron transfer number was determined using the Koutecky–Levich (K–L) method, based on LSV measurements recorded at rotation speeds of 400, 900, 1600, and 2400 rpm.[31] The reciprocal current density was plotted against the inverse square root of the rotation speed to obtain a linear relationship, from which n was calculated:

$$\frac{1}{j} = \frac{1}{j_k} + \frac{1}{j_l} = \frac{1}{j_k} + \frac{1}{0.62nFD^{2/3}\omega^{1/2}\mu^{-1/6}C_0} \quad (1)$$

where j_k and j_l denote the kinetic and diffusion-limited current densities, respectively; n is the number of electrons transferred; F is the Faraday constant (96 485 C mol^{-1}); C_0 is the bulk concentration of O_2 in the electrolyte (1.2×10^{-3} mol L^{-1}); D is the O_2 diffusion coefficient (1.9×10^{-5} cm^2 s^{-1}); μ is the kinematic viscosity of the electrolyte; and ω is the angular rotation speed of the disk (rad s^{-1}).

Electrochemical impedance spectroscopy (EIS) data were analyzed using ZView software. Nyquist plots were fitted using an equivalent circuit model comprising solution resistance (R_s), charge-transfer resistance (R_{ct}), and a constant-phase element (CPE), to account for non-ideal capacitive behavior associated with surface roughness and porosity. The current (J) and power densities generated by the MFC were calculated as follows:[30]

$$J(\text{mA m}^{-2}) = \frac{I}{A_{anode}} \quad (2)$$

$$P(\text{W m}^{-2}) = \frac{IV}{A_{anode}} \quad (3)$$

where I is the current, A_{anode} is the anode surface area, and V is the output voltage.

2.6. *Ab initio* calculations

Density functional theory (DFT) calculations were performed using the Vienna *Ab initio* Simulation Package (VASP).[32] The projector-augmented wave (PAW) method was used to describe the interaction between valence electrons and ionic cores, while exchange–correlation effects were treated using the Perdew–Burke–Ernzerhof (PBE) functional within the generalized gradient approximation.[33,34] A plane-wave cutoff energy of 520 eV was applied, and spin polarization was included (ISPIN = 2).

A Monkhorst–Pack grid of 3 × 3 × 1 was employed to sample the Brillouin zone.[35] Grimme's DFT-D3 correction with Becke–Johnson damping (IVDW = 11) was employed to account for long-range van der Waals interactions.[36] All structures were fully relaxed using the conjugate gradient algorithm until the residual forces were below 0.02 eV $Å^{-1}$. Initial magnetic moments were assigned as follows: Ti (2.0 μB), C (0.6 μB), Ni (2.0 μB), and Co (3.0 μB). Additional details regarding model construction and reaction energetics are provided in the SI.

3. Results and discussions

3.1. Catalyst properties

The XRD analysis confirms the successful transformation of Ti_3AlC_2 to $Ti_3C_2T_x$, as evidenced by the disappearance of the characteristic Al peak (014) at ~39°, attributed to the MAX phase (Fig. 2, green line).[37] Concurrently, a pronounced shift of the (002) peak toward lower 2θ values is observed after etching (Fig. 2, blue line), indicating an expansion of the interlayer spacing due to the removal of Al layers and subsequent introduction of surface terminations and intercalated species.[38] Additional reflections observed at ~16° and ~28° are assigned to the (004) and (006) planes of $Ti_3C_2T_x$, respectively, confirming the preservation of the layered $Ti_3C_2T_x$ structure and long-range

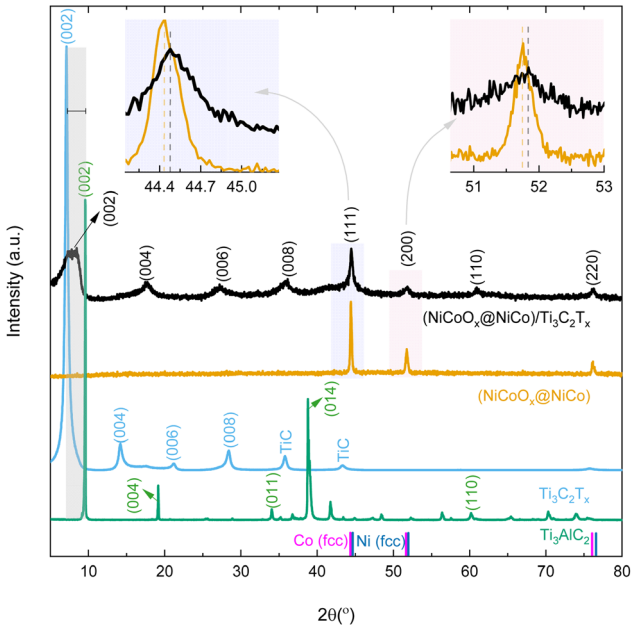

Fig. 2 XRD patterns of Ti_3AlC_2 (green line), $Ti_3C_2T_x$ (blue line), $NiCoO_x$@NiCo (orange line), and ($NiCoO_x$@NiCo)/$Ti_3C_2T_x$ (black line), along with reference patterns for fcc-Ni (blue vertical lines) and fcc-Co (magenta vertical lines). The right and left insets present magnified views of the (111) and (200) diffraction peaks, respectively, of the NiCo alloy in both $NiCoO_x$@NiCo and ($NiCoO_x$@NiCo)/$Ti_3C_2T_x$.

ordering along the *c*-axis after delamination.[37] A weak reflection around ~36° is attributed to TiC, an impurity originating from unreacted TiC during the synthesis of the MAX phase precursor.[39,40]

The $NiCoO_x$@NiCo catalyst exhibited distinct diffraction peaks at 44.44°, 51.75°, and 76.18°, corresponding to the (111), (200), and (220) planes, respectively (PDF: 04-004-8490), as illustrated in Fig. 2 (orange line). These peaks appeared between the corresponding peaks of fcc-Ni and fcc-Co (Fig. 2, blue and magenta reference lines), confirming the formation of a NiCo alloy.[41–44] Notably, no discernible peaks associated with crystalline $NiCoO_x$ are observed, suggesting that the oxide shell is either amorphous, poorly crystalline, or confined to a thin surface layer, and therefore contributes negligibly to the bulk diffraction signal.[45,46]

For the ($NiCoO_x$@NiCo)/$Ti_3C_2T_x$ heterostructure (Fig. 2, black line), the characteristic alloy peaks are retained at slightly shifted positions (44.49°, 51.84°, and 76.28°), alongside the diffraction features of $Ti_3C_2T_x$ shift to higher 2θ values, indicating a reduction in interlayer spacing. This behavior is attributed to partial removal or rearrangement of surface terminations (–OH, –O, –F) and the elimination of intercalated water during thermal treatment, leading to structural densification.[47] In addition, the (002) peak of $Ti_3C_2T_x$ becomes broader and less intense after nanoparticle deposition, indicating reduced crystallinity and partial structural disorder induced by nanoparticle anchoring and thermal processing.[48,49]

A closer examination of the alloy reflections (insets in Fig. 2) reveals slight positive shifts of ~0.05° and ~0.09° in the (111) and (200) planes, respectively, for the ($NiCoO_x$@NiCo)/$Ti_3C_2T_x$ heterostructure compared to $NiCoO_x$@NiCo. These shifts indicate lattice contraction, likely arising from interfacial electronic interactions between the NiCo alloy and the $Ti_3C_2T_x$ support, as well as possible charge-transfer effects involving surface terminations.[50] Based on the shift in the (111) reflection, the compressive lattice strain (ε_{111}) provides further evidence of strong coupling between the $NiCoO_x$@NiCo nanoparticles and the $Ti_3C_2T_x$ support.[51]

The STEM imaging and elemental mapping of $NiCoO_x$@NiCo reveal a broad nanoparticle size distribution ranging from 8.5 nm to 115 nm and an average diameter of ~35 nm (Fig. S1). The corresponding HAADF-STEM images (Fig. 3a–c) show well-defined nanoparticles with a clear core–shell architecture, consisting of a metallic NiCo core encapsulated by an ultrathin (~4 nm) oxide shell. Lattice-resolved imaging yields interplanar spacings of 0.216 nm and 0.188 nm, corresponding to the (111) and (200) planes of the NiCo alloy, respectively (Fig. 3c).[24,52]

Fast Fourier Transform (FFT) pattern acquired from the core of the particle displayed diffraction spots indexed to the (111) and (200) planes of the metallic NiCo alloy, consistent with cubic structure, $Fm\bar{3}m$ space group and lattice parameters $a = b = c = 3.54$ Å and $\alpha = \beta = \gamma = 90°$ (Fig. 3d), confirming its metallic nature. In contrast, FFT patterns obtained from the shell region (Fig. 3e) exhibit reflections consistent with a spinel $NiCoO_x$ phase indexed to the $Fd\bar{3}m$ space group, with lattice parameters $a = b = c = 8.065$ Å and $\alpha = \beta = \gamma = 90°$, verifying the formation of an oxide shell surrounding the alloy core.

STEM-EELS elemental mapping of the $NiCoO_x$@NiCo catalyst (Fig. 3f and k), further resolves the spatial distribution of elements within individual particles. Ni and Co signals exhibit strong spatial overlap, indicating homogeneous alloying within the core (Fig. 3g and h), while oxygen is predominantly localized at the particle periphery, forming an O-rich shell (Fig. 3i). The combined elemental maps clearly delineate a NiCo-rich core enclosed by a $NiCoO_x$ shell (Fig. 3j). Line-scan analysis confirms that both Ni and Co are present throughout the particle, with the core dominated by metallic species and the shell enriched in oxygen-coordinated Ni/Co species (Fig. 3k and l).

The HRTEM of a large area view of the $NiCoO_x$@NiCo (Fig. S2) demonstrates uniform particle dispersion, while additional EELS analyses (Fig. S3 and S4) reveal consistent elemental distributions across multiple particles, confirming the reproducibility of the core–shell structure. Trace amounts of boron (<2 at%) are detected at the particle surface, likely originating from the $NaBH_4$-assisted reduction process.

The formation of a well-defined metal/oxide core–shell architecture is expected to generate abundant interfacial sites between the conductive NiCo core and the redox-active $NiCoO_x$ shell. Such interfaces can facilitate efficient charge transport while providing active sites for oxygen adsorption and transformation, thereby modulating the adsorption energetics of reaction intermediates through interfacial electronic interactions.[24,53]

The HR-TEM analysis reveals that the $Ti_3C_2T_x$ consists of a few-layered ultrathin sheets (Fig. 4a and b), providing a suitable platform for nanoparticle anchoring. Upon integration,

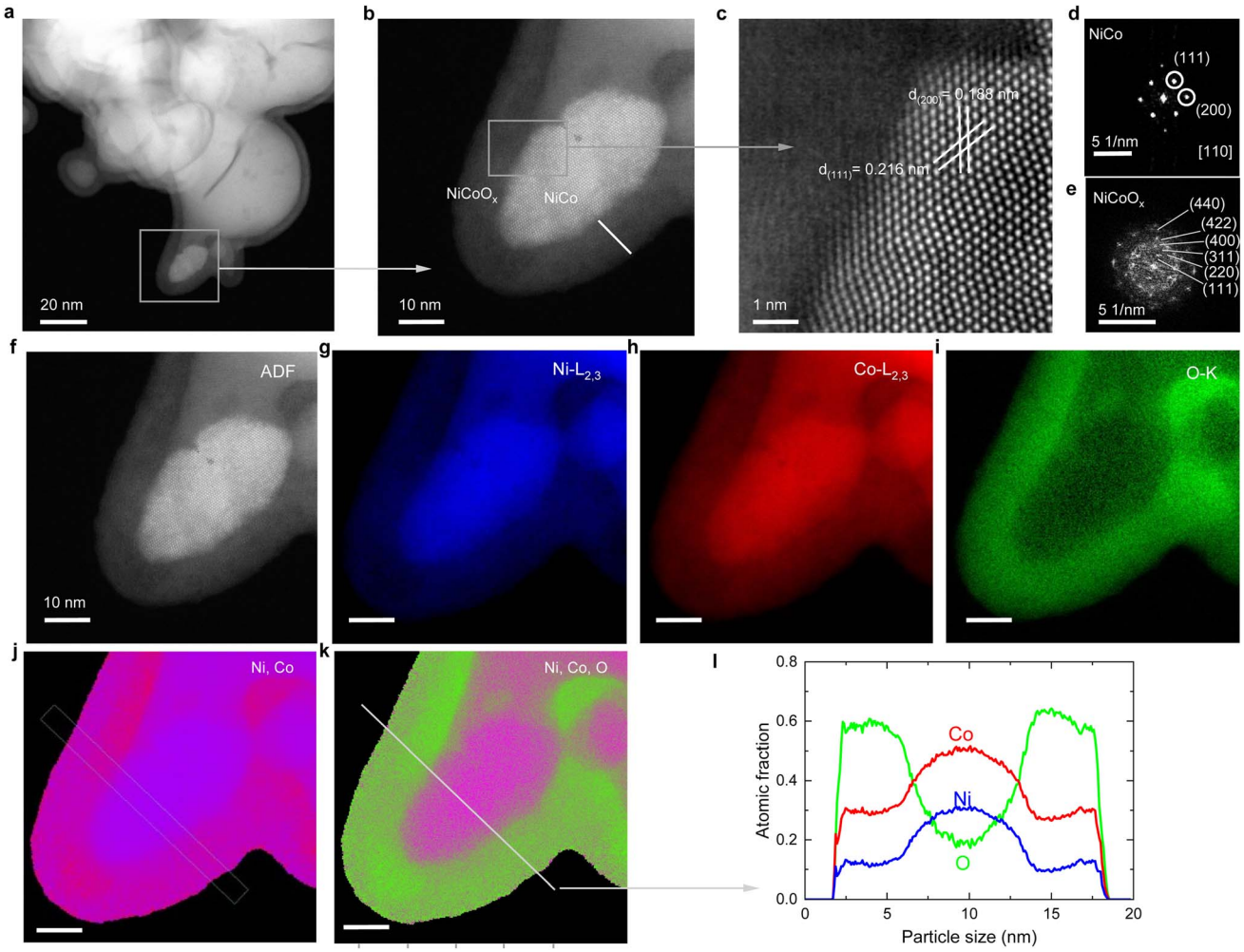

Fig. 3 (a) HAADF-STEM image of the NiCoO$_x$@NiCo catalyst. (b and c) HR-STEM images of a type-1 grain. (d and e) FFTs derived from the corresponding HR-STEM images: (d) NiCo alloy core and (e) NiCoO$_x$ shell. (f) ADF image of the type-1 grain. (g–i) EELS elemental maps of (g) Ni, (h) Co, (i) O, and (j) overlay elemental mapping of Ni and Co. (k) Overlay elemental mapping of Ni, Co, and O, and (l) corresponding atomic fraction profiles of Ni, Co, O obtained from the line scan indicated in (k). Abbreviations: HAADF-STEM, high-angle annular dark-field scanning transmission electron microscopy; HR-STEM, high-resolution STEM; FFT, fast Fourier transform; ADF, annular dark-field; EELS, electron energy loss spectroscopy.

NiCoO$_x$@NiCo nanoparticles are uniformly distributed across the $Ti_3C_2T_x$ surface, forming a well-defined heterostructure (Fig. 4c and d). This morphology confirms the successful assembly of core–shell NiCoO$_x$@NiCo nanoparticles onto the MXene support.

STEM-EDX elemental mapping of pristine $Ti_3C_2T_x$ (Fig. S5) shows a homogeneous distribution of Ti, C, O, and F, consistent with the expected surface terminations (–O and –F) introduced during synthesis. In the (NiCoO$_x$@NiCo)/$Ti_3C_2T_x$ heterostructure, STEM-EELS mapping (Fig. 4e–l) further confirms the co-localization of Ti, C, O, and F with Ni and Co, indicating successful integration of the nanoparticles without disrupting the MXene framework. This observation is consistent with the structural integrity inferred from XRD analysis (Fig. 2).

Nitrogen adsorption–desorption measurements reveal a significant increase in surface area upon heterostructure formation. Pristine $Ti_3C_2T_x$ exhibits a low specific surface area ($\sim$3 m^2 g^{-1}), in agreement with previous reports.[53] In contrast, the (NiCoO$_x$@NiCo)/$Ti_3C_2T_x$ composite displays a markedly higher surface area ($\sim$31 m^2 g^{-1}), approaching that of the NiCoO$_x$@NiCo component ($\sim$32 m^2 g^{-1}, Fig. S6). This enhancement is primarily attributed to the incorporation of the nanoparticulate phase, which introduces additional accessible surface sites and modifies the composite's overall textural properties.

The surface chemical states of Ni, Co, and other elements (Fig. 5 and S7) in the NiCo and (NiCoO$_x$@NiCo)/$Ti_3C_2T_x$ samples were analyzed by quasi *in situ* XPS after reduction at 400 °C under an H_2/Ar atmosphere. For the NiCoO$_x$@NiCo sample, the Ni 2p spectrum (Fig. 5a) exhibits a dominant peak at $\sim$852.6 eV corresponding to metallic Ni^0 (ref. 29, 54 and 55) together with an oxidized component centered at $\sim$856.2 eV and a pronounced shake-up satellite at $\sim$861.7 eV, indicating that Ni predominantly exists as Ni^{2+} species with a minor contribution

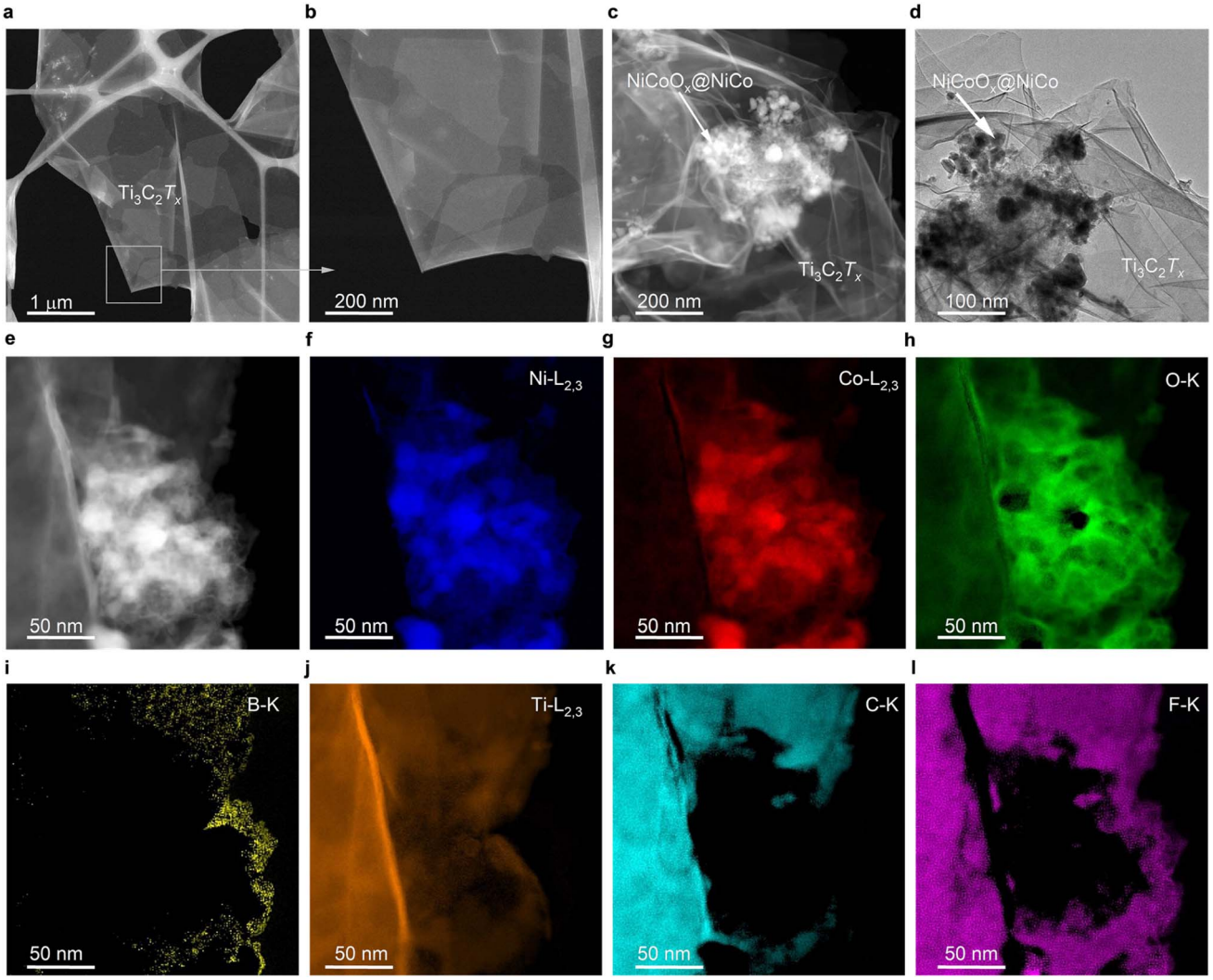

Fig. 4 (a and b) HAADF-STEM images of $Ti_3C_2T_x$. (c and d) HAADF-STEM and TEM images, respectively, of the ($NiCoO_x$@NiCo)/$Ti_3C_2T_x$ heterostructure. (e) ADF image of the ($NiCoO_x$@NiCo)/$Ti_3C_2T_x$ sample. (f–l) Corresponding EELS elemental maps for (f) B, (g) C, (h) O, (i) F, (j) Ti, (k) Co, and (l) Ni. Abbreviations: HAADF-STEM, high-angle annular dark-field scanning transmission electron microscopy; TEM, transmission electron microscopy; ADF, annular dark-field; EELS, electron energy loss spectroscopy.

from Ni^{3+}.[29,55] The Co 2p spectrum (Fig. 5b) shows a main Co $2p_{3/2}$ feature at ~781.8 eV accompanied by a satellite at ~786.8 eV, indicating oxidized cobalt species mainly attributed to Co^{2+} with a small contribution of Co^{3+}.[29,55] Meanwhile, the low-binding-energy peak at ~778.1 eV is assigned to metallic Co from the NiCo alloy.[29,55] The coexistence of metallic and oxidized Ni and Co species aligns with the STEM-EELS observations, confirming a metallic NiCo core encapsulated by an $NiCoO_x$ shell.

The ($NiCoO_x$@NiCo)/$Ti_3C_2T_x$ heterostructure exhibits similar spectral features are observed, with slight shifts in binding energy reflecting interfacial electronic interactions. The Ni 2p spectrum (Fig. 5c) indicates the coexistence of Ni^0 and Ni^{2+}/Ni^{3+} species, while the Co 2p spectrum (Fig. 5d) confirms that cobalt remains predominantly in the Co^{2+} state with minor Co^{3+} contribution. These results demonstrate that the heterostructure retains a mixed metallic, oxidized character, indicative of strong metal-oxide interfacial coupling. The Ti 2p (Fig. 5e) and C 1s (Fig. 5f) spectra confirm the preservation of the $Ti_3C_2T_x$ framework, with characteristic Ti–C bonding and partially oxidized Ti species (Ti^{2+}/Ti^{3+}/Ti–O), consistent with surface terminations introduced during synthesis.

Quantitative XPS analysis (Table S1) reveals an increased Co/Ni surface ratio and a reduced metallic fraction in the ($NiCoO_x$@NiCo)/$Ti_3C_2T_x$ catalyst compared to $NiCoO_x$@NiCo, indicating a higher proportion of oxidized surface species. This suggests that the $Ti_3C_2T_x$ support promotes the formation of oxidic interfacial species, consistent with $NiCoO_x$-like surface phases and in agreement with HAADF-STEM-EELS observations (Fig. 3 and 4). This finding demonstrates that the surface of $NiCoO_x$@NiCo is dominated by Co^{2+} and Ni^{2+} states, with minor amounts of Co^{3+}/Ni^{3+}, indicating a chemically and electronically heterogeneous surface. The mixed-valence chemical state is further supported by EPR analysis (Fig. S8). The $NiCoO_x$@NiCo sample exhibits a broad

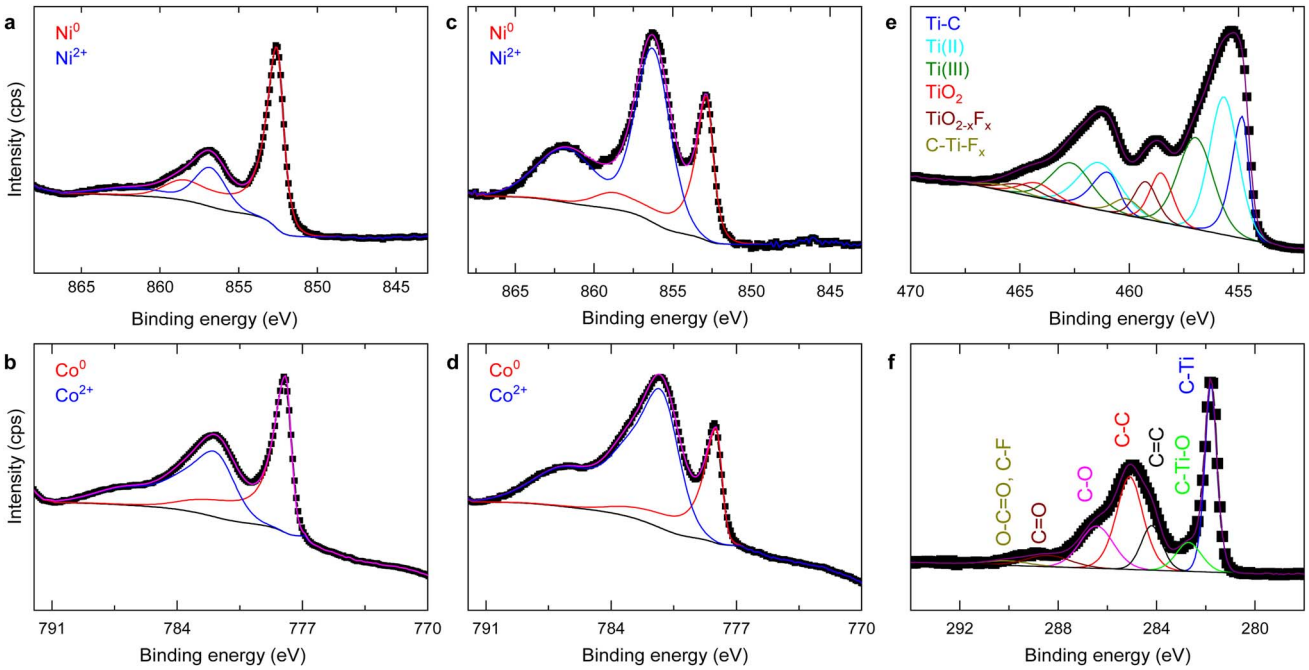

Fig. 5 XPS spectra of the $NiCoO_x$@NiCo catalyst: (a) Ni 2p, (b) Co 2p, and of the ($NiCoO_x$@NiCo)/$Ti_3C_2T_x$ catalyst: (c) Ni 2p, (d) Co 2p, (e) Ti 2p, (f) C 1s. Abbreviation: XPS, X-ray photoelectron spectroscopy.

signal characteristic of strong magnetic exchange interactions, covering almost the entire range of the magnetic field sweep (around 7000 G), indicating coupling between transition metal centers *via* super exchange pathways (Co–O–Co and Co–O–Ni).[56,57] In contrast, the ($NiCoO_x$@NiCo)/$Ti_3C_2T_x$ sample displays a well-defined Co^{2+} signal ($g \approx 2.155$), suggesting reduced magnetic coupling due to improved dispersion of active species on the $Ti_3C_2T_x$ support.[58,59] Compositional analysis of the samples using ICP (Table S2) confirmed the presence of both Ni and Co, with a Co/Ni ratio of 1.07 and 1.03 for $NiCoO_x$@NiCo and ($NiCoO_x$@NiCo)/$Ti_3C_2T_x$, respectively.

3.2. Electrochemical testing

The CV curves of all catalysts were recorded under an Ar atmosphere, showing similar capacitive behavior and reflecting comparable electrolyte environments (Fig. S9). In contrast, under O_2-saturated conditions, the ($NiCoO_x$@NiCo)/$Ti_3C_2T_x$ catalyst exhibits a markedly enhanced ORR response, delivering a higher cathodic peak current density (-3.5 mA cm^{-2} at 0.74 V) compared to $NiCoO_x$@NiCo (-1.24 mA cm^{-2} at 0.75 V) and $Ti_3C_2T_x$ (-0.35 mA cm^{-2} at 0.70 V) (Fig. 6a). This enhancement indicates improved catalytic activity and facilitates oxygen reduction kinetics.

Notably, the ($NiCoO_x$@NiCo)/$Ti_3C_2T_x$ achieves a higher peak current density than commercial 10 wt% Pt/C under identical conditions, while exhibiting a comparable reduction potential ($\Delta E \approx 0.01$ V) (Fig. S10a). This suggests that the heterostructure provides competitive intrinsic activity, while the enhanced current response reflects improved charge transport and utilization of active sites.[19,25]

LSV measurements at 1600 rpm further confirm the heterostructure's superior ORR performance. The ($NiCoO_x$@NiCo)/$Ti_3C_2T_x$ catalyst exhibits a half-wave potential ($E_{1/2}$) of 0.79 V and a limiting current density of -4.16 mA cm^{-2}, compared to 0.77 V and -3.98 mA cm^{-2} for $NiCoO_x$@NiCo, and 0.80 V and -2.65 mA cm^{-2} for Pt/C (Fig. 6b). All catalysts significantly outperform pristine $Ti_3C_2T_x$ (0.66 V and -0.26 mA cm^{-2}), highlighting the importance of heterostructure formation. The comparable half-wave potentials suggest similar intrinsic ORR kinetics, while the higher limiting current density of the heterostructure indicates enhanced mass transport and/or increased electrochemically accessible surface sites.

To further evaluate the active surface characteristics, the electrochemically active surface area (ECSA) was estimated from the double-layer capacitance (C_{dl}) obtained *via* CV in the non-faradaic region (0.0–0.10 V *vs.* RHE) (Fig. S11 and S12). The ($NiCoO_x$@NiCo)/$Ti_3C_2T_x$ catalyst exhibits the highest C_{dl} value (375.2 μF cm^{-2}), followed by $NiCoO_x$@NiCo (316.5 μF cm^{-2}), Pt/C (230.0 μF cm^{-2}), and $Ti_3C_2T_x$ (225.6 μF cm^{-2}). The increased C_{dl} of the heterostructure indicates a larger electrochemically accessible surface area, thereby enhancing ORR activity.

The electron transfer number (n) per oxygen molecule during the ORR was determined using the K–L method, from LSV curves acquired during the rotating disk electrode measurements at varying rotation speeds (400, 900, 1600, and 2400 rpm) (Fig. 7a–c). The increase in limiting current density with rotation speed reflects enhanced mass transport, arising from the thinning of the diffusion layer and improved O_2 flux to the catalyst surface.[60,61] K–L plots derived from the LSV data exhibit good linearity, indicating first-order reaction kinetics with respect to dissolved oxygen and validating the reliability of the

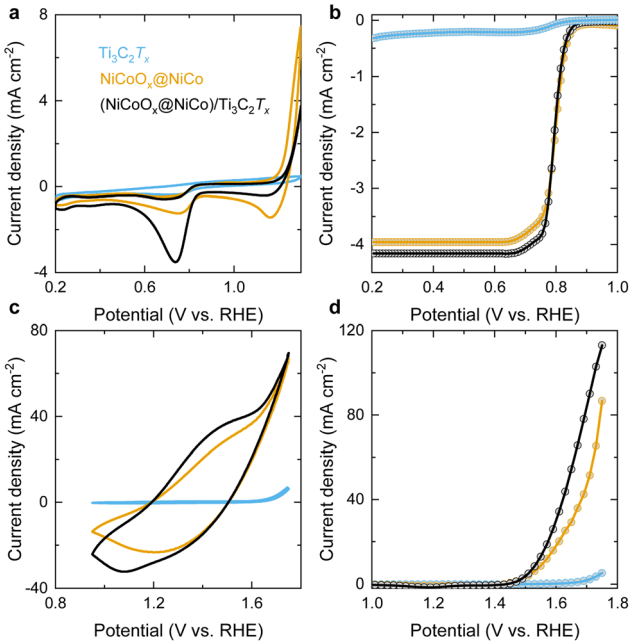

Fig. 6 Electrochemical performance of the catalysts (a and b) in the ORR: (a) CV and (b) LSV results, and in the (c and d) OER: (c) CV and (d) LSV results. Abbreviations: RHE, reversible hydrogen electrode; ORR, oxygen reduction reaction; OER, oxygen evolution reaction; CV, cyclic voltammetry; LSV, linear sweep voltammetry.

analysis. The electron transfer number was calculated from the slope of the K–L plots within the mixed kinetic-diffusion region (0.4–0.6 V *vs.* RHE).[62]

The ($NiCoO_x$@NiCo)/$Ti_3C_2T_x$ catalyst displays an electron transfer number of ~3.98, approaching the ideal four-electron pathway for direct reduction of O_2 to OH^-. In comparison, $NiCoO_x$@NiCo exhibits a lower value (~3.7), while pristine $Ti_3C_2T_x$ shows a value of ~2, indicative of a two-electron pathway leading to peroxide intermediates (Fig. 7d).[63]

A 10 h chronoamperometric stability test under ORR conditions demonstrates that the ($NiCoO_x$@NiCo)/$Ti_3C_2T_x$ catalyst maintains >98% of its initial limiting current density, with no observable change in onset potential (Fig. S13). A slight negative shift in the half-wave potential (0.79 to 0.74 V) is observed, indicating minor changes in intrinsic ORR kinetics while preserving overall catalytic stability.

To further contextualize the catalytic behavior, the materials were also evaluated for OER. The ($NiCoO_x$@NiCo)/$Ti_3C_2T_x$ catalyst exhibits enhanced OER activity compared to its individual components, delivering higher current densities at comparable overpotentials (Fig. 6c and d). In contrast, $Ti_3C_2T_x$ alone shows negligible activity, confirming its limited intrinsic reactivity toward oxygen electrochemistry and highlighting the critical role of the $NiCoO_x$@NiCo phase.

The EIS was employed to probe charge-transfer characteristics under ORR conditions. All catalysts exhibit comparable solution resistance ($R_s \approx 0.26$–$0.54\ \Omega$), indicating similar electrolyte environments (Fig. 8a). The charge-transfer resistance (R_{ct}) follows the trend: $Ti_3C_2T_x$ < ($NiCoO_x$@NiCo)/$Ti_3C_2T_x$ < $NiCoO_x$@NiCo. Despite a slightly higher R_{ct} than pristine $Ti_3C_2T_x$, the heterostructure demonstrates improved overall electrochemical performance, suggesting that factors beyond

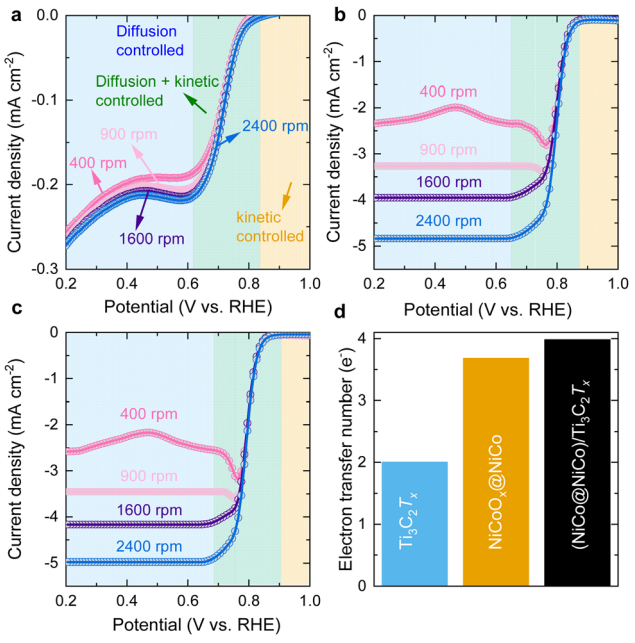

Fig. 7 LSV curves recorded at varying rotation speeds for the (a) $Ti_3C_2T_x$, (b) $NiCoO_x$@NiCo, and (c) ($NiCoO_x$@NiCo)/$Ti_3C_2T_x$ catalysts. (d) Electron transfer numbers of the catalysts were calculated using the K–L method. Abbreviations: LSV, linear sweep voltammetry; K–L, Koutecky–Levich; RHE, reversible hydrogen electrode.

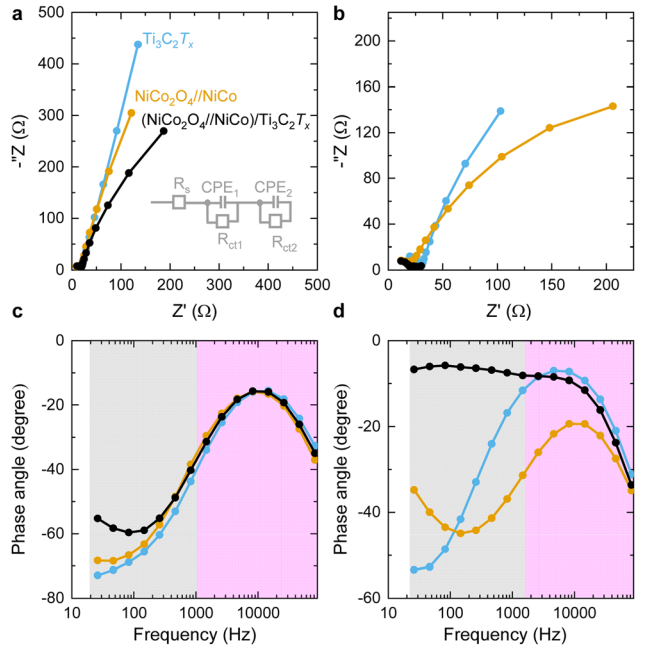

Fig. 8 (a) EIS curve for the ORR; inset depicts the equivalent circuit model used to fit the EIS data. (b) EIS curve for the OER. (c) Bode phase angle plot for the ORR. (d) Bode plot for the OER. Abbreviations: EIS, electrochemical impedance spectroscopy; ORR, oxygen reduction reaction; OER, oxygen evolution reaction.

simple charge-transfer resistance, such as active site density and interfacial electronic effects, govern ORR activity.[64–66]

The Bode phase-angle plot (Fig. 8c) of ORR provides further insight into frequency-dependent charge-transfer behavior. Notably, the observed negative phase angles are typical in EIS measurements of ORR/OER electrodes and arise from the capacitive nature of the electrode/electrolyte interface, where charge is stored through double-layer charging, and the adsorption of surface reaction intermediates.[67] In the plot, the high-frequency region (Fig. 8c, pink region) corresponds to electron transfer, while the low-frequency region (gray area) reflects interfacial mass transfer processes.[68] The ($NiCoO_x$@-NiCo)/$Ti_3C_2T_x$ catalyst exhibits a lower phase angle (−55.23°) at low frequencies (100–103 Hz) and an intermediate phase angle (−15.97°) at high frequencies (10^3–10^4 Hz), indicating efficient mass transport and faster electron transport. The ORR catalytic activity of the catalysts can be ranked as $Ti_3C_2T_x$ > ($NiCoO_x$@-NiCo)/$Ti_3C_2T_x$ > $NiCoO_x$@NiCo. This behavior is attributed to the high electrical conductivity of $Ti_3C_2T_x$, which facilitates charge transport.[69]

Furthermore, EIS measurements under OER conditions yielded comparable R_s values across all three catalysts (2.4–3.9 Ω), indicating a uniform electrolyte environment. The ($NiCoO_x$@NiCo)/$Ti_3C_2T_x$ catalyst exhibits the lowest R_{ct} value (16.7 Ω), indicating enhanced interfacial charge-transport. The Bode phase angle plot shows a peak in the high-frequency region (10^3–10^4 Hz) (Fig. 8d), associated with the local electron transfer process.[70] The $NiCoO_x$@NiCo exhibited a higher phase angle (−19.33°) in this region, suggesting slower electron transport. In contrast, $Ti_3C_2T_x$ exhibits the highest phase angle (−7.23°), followed by ($NiCoO_x$@NiCo)/$Ti_3C_2T_x$ (−9.28°), suggesting that the incorporation of $Ti_3C_2T_x$ facilitates faster electron transport.[66]

Further analysis of EIS data for both OER and ORR using the Bode magnitude plot (Fig. S14) revealed reaction-dependent impedance behavior for OER. ($NiCoO_x$@NiCo)/$Ti_3C_2T_x$ exhibits the lowest impedance, indicating accelerated interfacial charge transfer and improved electron/ion transport due to the coupling between conductive $Ti_3C_2T_x$ and $NiCoO_x$@NiCo active sites. For ORR, $NiCoO_x$@NiCo exhibits the lowest impedance, suggesting that while $Ti_3C_2T_x$ improves the overall conductivity and interfacial response, the ORR process may be more strongly governed by the intrinsic $NiCoO_x$@NiCo active phase.[67]

The observed catalytic behavior arises from the synergistic interplay of multiple factors. XPS analysis indicates a Co-enriched surface with mixed oxidation states (Co^{2+}/Co^{3+}) alongside metallic NiCo, providing a redox-flexible environment for oxygen electrocatalysis. The coexistence of Ni^{2+}/Ni^{3+} and Co^{2+}/Co^{3+} species facilitates the adsorption and transformation of oxygenated intermediates, while the metallic core ensures efficient electron transport. In combination with strong interfacial electronic coupling with $Ti_3C_2T_x$ these features collectively enhance the catalytic performance.[71–76]

3.3. *Ab initio* calculations

Several Ti_3C_2 slabs: pristine (Fig. S15a), O-functionalized (Fig. S15b), OH-functionalized (Fig. S15c), and F-functionalized (Fig. S15d), were prepared for the DFT simulation. To elucidate the origin of the observed catalytic activity, NiCo-decorated $Ti_3C_2T_x$ models were investigated, with Ni and Co treated as active sites (Fig. S16). It is important to note that the DFT model employs a simplified Ni–Co double-atom catalyst (DAC) configuration containing one Ni and one Co atom. This model is designed to probe local active-site chemistry and intrinsic catalytic roles, rather than to reproduce the exact experimental Ni/Co ratio. Therefore, the calculations provide mechanistic insight into site-specific activity, independent of the macroscopic elemental composition.

Fig. 9 and S17 illustrate the thermodynamic reaction profiles for the ORR and OER, respectively. Notably, ORR and OER are reverse electrochemical processes that proceed through the same adsorbed intermediates (*OOH, *O, and *OH), but in opposite directions. Consequently, the catalytic performance in both reactions is governed by the ability of the catalyst to balance the adsorption energies of the shared intermediates.

Bare and functionalized Ti_3C_2 surfaces exhibit strong overbinding of key intermediates (*O and *OH), leading to excessive exergonic adsorption and large uphill steps (ΔG > 2.0 eV). This imbalance results in sluggish ORR kinetics and prohibitively high OER overpotentials, aligning with previous reports indicating that $Ti_3C_2T_x$ is intrinsically a poor ORR/OER catalyst due to its inability to balance adsorption–desorption energetics.[77] Although bare and functionalized MXenes (Ti_3C_2, O-Ti_3C_2, OH-Ti_3C_2, and F-Ti_3C_2) exhibit highly exergonic ORR energetics (Fig. 9b), the adsorption energies of key intermediates remained excessively large, undermining the thermodynamic feasibility. For instance, *OOH adsorption energies reached −1.65 eV for Ti_3C_2, −1.45 eV for O-Ti_3C_2, and −1.40 eV for OH-Ti_3C_2, while the *OH adsorption energy for F-Ti_3C_2 was as low as −2.15 eV (Table S3). Such low potential reflects severe overbinding, particularly of *OH, which may poison the active sites and suppress catalytic turnover. Further, the OER profiles (Fig. S17a) exhibited prohibitively large uphill steps. Notably, the *OH → *O transition represents the most endergonic step, with ΔG values of 2.04 eV for O-Ti_3C_2, 2.15 eV for Ti_3C_2, and 1.92 eV for OH-Ti_3C_2. These substantial energy barriers correspond to high theoretical overpotentials (>0.9 V), thereby rendering these surfaces ineffective for the OER. This analysis confirms that bare Ti_3C_2, despite its strong oxygen affinity, is an intrinsically poor ORR and OER electrocatalyst owing to its inability to balance the energetics of adsorption and desorption of intermediates.[63]

Upon NiCo incorporation, the thermodynamic profiles are significantly improved. Structural optimization reveals stable adsorption of *OOH, *O, and *OH intermediates across both Ni and Co sites, with *OOH frequently relaxing into bridge configurations, indicating cooperative interaction between the two metals (Fig. S17). To distinguish their catalytic roles, two configurations were analyzed: (i) NiCo@Ni, considering Ni as an active site, and (ii) NiCo@Co, considering Co as an active site. The results reveal a clear functional asymmetry: in the Ni-centered ORR pathway (Fig. 9c), Ni sites reduced *OH binding energies to moderate values (*e.g.*, −0.80 to −1.70 eV), in contrast to the excessively high adsorption energies observed for bare Ti_3C_2. In parallel, the initial O_2 activation step ($+O_2$ → *OOH)

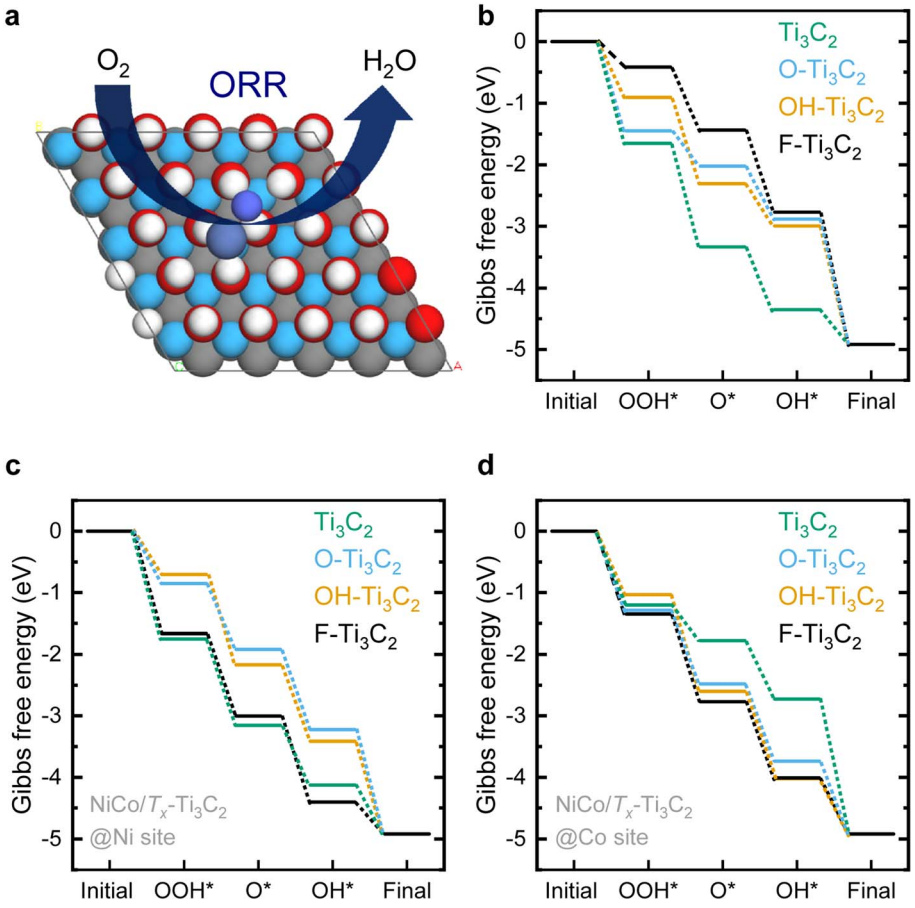

Fig. 9 (a) Representative geometry of the catalyst system. The red, white, gray, blue, and purple spheres represent oxygen, hydrogen, carbon, titanium, and NiCo, respectively. (b) ORR free energy profiles for bare and functionalized MXenes (Ti_3C_2, O-Ti_3C_2, OH-Ti_3C_2, F-Ti_3C_2). (c and d) Free energy profiles of NiCo-decorated Ti_3C_2-based MXene with various terminations: (c) NiCo@Ni and (d) NiCo@Co systems.

became less exergonic, with ΔG ranging from −0.85 to −1.75 eV. In the Co-centered ORR pathway (Fig. 9d), Co sites exhibit more balanced adsorption of *O and *OH intermediates, resulting in smoother free-energy profiles and lower thermodynamic barriers (Table S3).

Notably, the Co-centered ORR pathway exhibits reaction steps closer to the ideal thermodynamic value (∼−1.23 eV per step), indicating superior catalytic efficiency for oxygen intermediate transformation. Similarly, for OER, the NiCo@Co configuration significantly lowers the rate-limiting step (*O → *OOH, $\Delta G \approx +1.03$ eV), corresponding to a low theoretical overpotential (∼0.20 V). These results demonstrate that Ni and Co cooperatively connect ORR and OER pathways through complementary roles: Ni promotes ORR initiation *via* *OOH stabilization, while Co governs the energetics of *O and *OH intermediates, which are critical for both ORR progression and OER rate-determining steps. This synergy enables a balanced adsorption–desorption landscape, which is essential for efficient bifunctional catalysis. Importantly, this DFT-derived mechanism is fully consistent with experimental observations. XPS (Fig. 5) and STEM analysis (Fig. 3) reveal a Co-enriched surface composition, while the DFT results identify Co as the more active site for oxygen intermediate binding.

3.4. Bioelectrochemical tests

The bioelectrochemical performance of the catalysts was evaluated in air-cathode MFCs over an extended 800 h operating period. The temporal evolution of anode potential (Fig. S18) and open-circuit voltage (OCV) (Fig. 10a) shows an inverse relationship, where a decrease in anode potential corresponds to an increase in OCV, reflecting electron accumulation at the anode. A transient drop in OCV at ∼400 h coincides with electrolyte replacement, after which both OCV and electrode potentials stabilize over subsequent operation cycles.

Following stabilization, polarization measurements were conducted. The ($NiCoO_x$@NiCo)/$Ti_3C_2T_x$ cathode achieves a higher operating potential (360 mV) compared to $NiCoO_x$@-NiCo (280 mV) (Fig. 10a). Correspondingly, the heterostructure delivers an enhanced current density (4.5 A m^{-2}) and maximum power density (1.6 W m^{-2}), exceeding those of $NiCoO_x$@NiCo (2.9 A m^{-2} and 0.9 W m^{-2}, respectively) (Fig. 10b). The internal resistance, estimated from the slope of the polarization curve, is lower for the ($NiCoO_x$@NiCo)/$Ti_3C_2T_x$ based MFC (67.84 Ω) than for $NiCoO_x$@NiCo (90.17 Ω) (Fig. 10c and d), indicating improved charge transport and reduced ohmic losses.[76] Collectively, these results demonstrate the superior cathodic

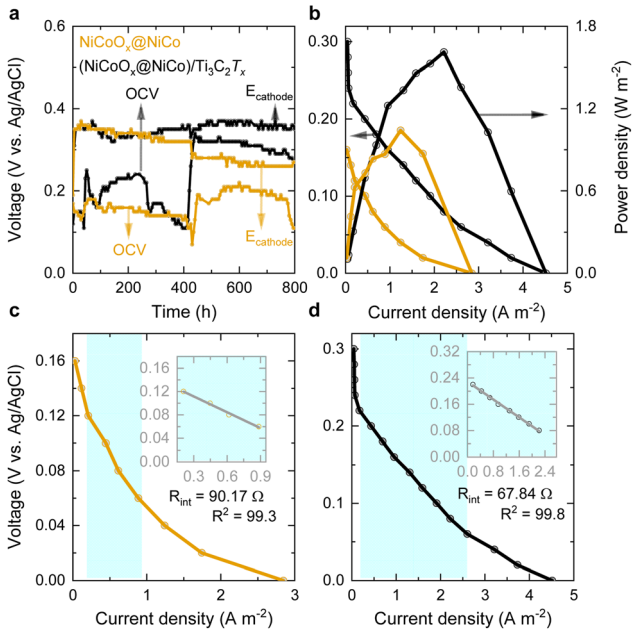

Fig. 10 (a) Long-term MFC operation over 800 h. (b) Polarization and power density curves of MFC incorporating the NiCoO$_x$@NiCo and (NiCoO$_x$@NiCo)/Ti$_3$C$_2$T$_x$ cathodes. (c and d) R_{int} of MFC incorporating the NiCoO$_x$@NiCo and (NiCoO$_x$@NiCo)/Ti$_3$C$_2$T$_x$ cathodes, respectively. Abbreviations: R_{int}, internal resistance; MFC, microbial fuel cell; OCV, open-circuit voltage.

performance of the heterostructure relative to the single-phase catalyst and place it among competitive platinum-group-metal-free systems.[78–81]

The SEM analysis of the used anode reveals comparable biofilm coverage for both systems (Fig. S19), indicating that the observed performance differences originate primarily from cathode properties rather than biological variability. The enhanced activity of the (NiCoO$_x$@NiCo)/Ti$_3$C$_2$T$_x$ catalyst can be attributed to the synergistic interplay between its components. Mixed-valence Co species (Co^{2+}/Co^{3+}) provide redox-active sites for oxygen intermediate adsorption, while Ni contributes to electronic modulation and stabilization of reaction intermediates. In parallel, the conductive Ti$_3$C$_2$T$_x$ scaffold facilitates efficient electron transport and promotes strong interfacial coupling with the NiCoO$_x$@NiCo phase. This integrated design enables improved ORR kinetics and charge-transfer efficiency under neutral conditions, highlighting the potential of MXene-based heterostructures as effective cathode catalysts for sustainable energy generation in microbial fuel cells.

4. Conclusions

This study presents a rationally engineered (NiCoO$_x$@NiCo)/Ti$_3$C$_2$T$_x$ heterostructure catalyst for ORR under neutral-pH conditions, directly addressing the critical requirements of MFCs. Compared with pristine Ti$_3$C$_2$T$_x$, the heterostructure exhibits markedly enhanced ORR activity, characterized by a higher limiting current density and reduced overpotential, indicative of accelerated reaction kinetics and a more favorable oxygen reduction pathway in neutral electrolyte.

Comprehensive structural and spectroscopic analyses unequivocally confirm the formation of a well-defined NiCoO$_x$@NiCo core–shell architecture uniformly anchored on conductive Ti$_3$C$_2$T$_x$ sheets. The synergistic coexistence of metallic NiCo cores and oxidized NiCoO$_x$ shells, coupled with strong interfacial electronic interactions with the Ti$_3$C$_2$T$_x$ support, facilitates rapid charge transport, maximizes active-site exposure, and optimizes the adsorption energetics of oxygen intermediates. Complementary DFT calculations provide mechanistic insight, revealing a distinct functional synergy between Ni and Co active centers: Ni preferentially stabilizes *OOH intermediates, while Co regulates *O and *OH binding. This cooperative interplay effectively modulates the local electronic structure of Ti$_3$C$_2$T$_x$, alleviates its intrinsic overbinding limitations, and establishes a balanced adsorption–desorption landscape essential for efficient ORR under neutral conditions.

In the real air-cathode MFC, the (NiCoO$_x$@NiCo)/Ti$_3$C$_2$T$_x$ electrode achieves a high current density of 4.5 A m^{-2} and a peak power density exceeding 1.6 W m^{-2}, outperforming both pristine Ti$_3$C$_2$T$_x$ and benchmark NiCo-based catalysts. These results not only demonstrate the practical viability of the proposed catalyst in wastewater-driven bioelectrochemical systems, but also highlight the effectiveness of integrating Ti$_3$C$_2$T$_x$ conductivity, core–shell chemistry, and interfacial electronic tuning as a unified strategy for advancing neutral-pH electrocatalysis.

Conflicts of interest

The authors declare no conflict of interest.

Data availability

The data will be available upon reasonable request.

The data supporting this article have been included as part of the supplementary information (SI). Supplementary information is available. See DOI: https://doi.org/10.1039/d6ta03240k.

Acknowledgements

This research was supported by King Abdullah University of Science and Technology (KAUST, BAS/1/1403). The authors thank Dr Ananda Rao Hari for providing wastewater from the KAUST wastewater treatment facility.

References

1 Y. Zhao, D. P. Adiyeri Saseendran, C. Huang, C. A. Triana, W. R. Marks, H. Chen, H. Zhao and G. R. Patzke, *Chem. Rev.*, 2023, **123**, 6257–6358.
2 Z. F. Huang, J. Wang, Y. Peng, C. Y. Jung, A. Fisher and X. Wang, *Adv. Energy Mater.*, 2017, **7**, 1700544.
3 M. David, C. Ocampo-Martínez and R. Sánchez-Peña, *J. Energy Storage*, 2019, **23**, 392–403.

4 N. Du, C. Roy, R. Peach, M. Turnbull, S. Thiele and C. Bock, *Chem. Rev.*, 2022, **122**, 11830–11895.
5 J. Pak, W. Chang, C. H. Kwon and J. Cho, *Adv. Funct. Mater.*, 2025, **35**, 2415933.
6 S. Gupta, A. Patro, Y. Mittal, S. Dwivedi, P. Saket, R. Panja, T. Saeed, F. Martínez and A. K. Yadav, *Sci. Total Environ.*, 2023, **879**, 162757.
7 M. A. Aminudin, S. K. Kamarudin, B. H. Lim, E. H. Majilan, M. S. Masdar and N. Shaari, *Int. J. Hydrogen Energy*, 2023, **48**, 4371–4388.
8 Q. Wang, S. Kaushik, X. Xiao and Q. Xu, *Chem. Soc. Rev.*, 2023, **52**, 6139–6190.
9 B. E. Logan, *Appl. Microbiol. Biotechnol.*, 2010, **85**, 1665–1671.
10 J. V. Boas, V. B. Oliveira, M. Simões and A. M. F. R. Pinto, *J. Environ. Manage.*, 2022, **307**, 114525.
11 M. D. Bhatt and J. Y. Lee, *Energy Fuels*, 2020, **34**, 6634–6695.
12 X. Tian, X. F. Lu, B. Y. Xia and X. W. Lou, *Joule*, 2020, **4**, 45–68.
13 X. X. Wang, J. Sokolowski, H. Liu and G. Wu, *Chin. J. Catal.*, 2020, **41**, 739–755.
14 T. Toda, H. Igarashi and M. Watanabe, *J. Electrochem. Soc.*, 1998, **145**, 4185–4188.
15 X. Chia and M. Pumera, *Nat. Catal.*, 2018, **1**, 909–921.
16 F. R. Fan, R. Wang, H. Zhang and W. Wu, *Chem. Soc. Rev.*, 2021, **50**, 10983–11031.
17 Q. Fu, J. Han, X. Wang, P. Xu, T. Yao, J. Zhong, W. Zhong, S. Liu, T. Gao, Z. Zhang, L. Xu and B. Song, *Adv. Mater.*, 2021, **33**(6), 1907818.
18 Y. Wang, M. Zhang, Y. Liu, Z. Zheng, B. Liu, M. Chen, G. Guan and K. Yan, *Adv. Sci.*, 2023, **10**(13), 2207519.
19 A. Thakur, Y. Zhang, Y. Gogotsi and B. Anasori, *MRS Energy Sustainability*, 2025, **12**, 270–282.
20 B. Anasori and Y. Gogotsi, *Graphene 2D Mater.*, 2022, **7**, 75–79.
21 X. Wang, D. Luo, J. Wang, Z. Sun, G. Cui, Y. Chen, T. Wang, L. Zheng, Y. Zhao, L. Shui, G. Zhou, K. Kempa, Y. Zhang and Z. Chen, *Angew. Chem., Int. Ed.*, 2021, **60**, 2371–2378.
22 M. Hu, L. Chen, Y. Wang, J. Dai, Y. Bi, Y. Li, J. Zhao, G. Li, L. Wang, A. Meng and Z. Li, *J. Chem. Eng.*, 2025, **513**, 162785.
23 Y. Guan, Y. Cong, R. Zhao, K. Li, X. Li, H. Zhu, Q. Zhang, Z. Dong and N. Yang, *Small*, 2023, **19**, 2301276.
24 H. Xu, Z. X. Shi, Y. X. Tong and G. R. Li, *Adv. Mater.*, 2018, **30**, 1705442.
25 C. Chen, H. Su, L. N. Lu, Y. S. Hong, Y. Chen, K. Xiao, T. Ouyang, Y. Qin and Z. Q. Liu, *Chem. Eng. J.*, 2021, **408**, 127814.
26 P. D. Kolubah, H. O. Mohamed, A. R. Hari, Y. Ping, M. Ben Hassine, P. Dally, M. Obaid, X. Xu, J. K. El-Demellawi, P. E. Saikaly, M. Lanza, N. Ghaffour and P. Castaño, *Small*, 2024, 2406223.
27 J. Wu, P. Li, Y. T. Pan, S. Warren, X. Yin and H. Yang, *Chem. Soc. Rev.*, 2012, **41**, 8066–8074.
28 C. Wu, H. Li, H. He, Y. Song, C. Bi, W. Du and H. Xia, *ACS Appl. Mater. Interfaces*, 2019, **11**, 46902–46911.
29 M. C. Biesinger, B. P. Payne, A. P. Grosvenor, L. W. M. Lau, A. R. Gerson and R. S. C. Smart, *Appl. Surf. Sci.*, 2011, **257**, 2717–2730.
30 B. E. Logan, B. Hamelers, R. Rozendal, U. Shroder, J. Kelle, S. Freguia, P. Aelterman, W. Verstraete and K. Rabaey, *Environ. Sci. Technol.*, 2006, **40**, 5181–5192.
31 R. Zhou, Y. Zheng, M. Jaroniec and S. Z. Qiao, *ACS Catal.*, 2016, **6**, 4720–4728.
32 G. Kresse and J. Furthmüller, *Phys. Rev. B:Condens. Matter Mater. Phys.*, 1996, **54**, 11169.
33 P. E. Blöchl, *Phys. Rev. B:Condens. Matter Mater. Phys.*, 1994, **50**, 17953.
34 J. P. Perdew, K. Burke and M. Ernzerhof, *Phys. Rev. Lett.*, 1996, **77**, 3865.
35 H. J. Monkhorst and J. D. Pack, *Phys. Rev. B:Condens. Matter Mater. Phys.*, 1976, **13**, 5188.
36 S. Grimme, J. Antony, S. Ehrlich and H. Krieg, *J. Chem. Phys.*, 2010, **132**, 154104, DOI: 10.1063/1.3382344/926936.
37 K. R. G. Lim, M. Shekhirev, B. C. Wyatt, B. Anasori, Y. Gogotsi and Z. W. Seh, *Nat. Synth.*, 2022, **1**, 601–614.
38 A. Thakur, N. Chandran B. S., K. Davidson, A. Bedford, H. Fang, Y. Im, V. Kanduri, B. C. Wyatt, S. K. Nemani, V. Poliukhova, R. Kumar, Z. Fakhraai and B. Anasori, *Small Methods*, 2023, **7**, 2300030.
39 X. Wang, X. Fan, M. Li, W. Zhu, J. Xue, F. Ye and L. Cheng, *Ceram. Int.*, 2021, **47**, 13628–13634.
40 M. Downes, C. E. Shuck, B. McBride, J. Busa and Y. Gogotsi, *Nat. Protoc.*, 2024, **19**, 1807–1834.
41 B. Zhang, X. Zhang, Y. Wei, L. Xia, C. Pi, H. Song, Y. Zheng, B. Gao, J. Fu and P. K. Chu, *J. Alloys Compd.*, 2019, **797**, 1216–1223.
42 S. Huang, W. Zhang, Q. Chen, S. Zhou, L. Sun, L. Sha, G. Zhuang, P. Wang and X. Han, *Chem.–Eur. J.*, 2023, **29**, e202300321.
43 L. Wang, B. Wen, X. Bai, C. Liu and H. Yang, *ACS Appl. Nano Mater.*, 2019, **2**, 7827–7838.
44 M. Cheng, M. Wen, S. Zhou, Q. Wu and B. Sun, *Inorg. Chem.*, 2012, **51**, 1495–1500.
45 J. Fan, H. Zheng, A. Chen, L. Gu, X. Xie, J. Fan and Z. Ding, *Chem. Eng. J.*, 2023, **476**, 146638.
46 X. Yan, K. Li, L. Lyu, F. Song, J. He, D. Niu, L. Liu, X. Hu and X. Chen, *ACS Appl. Mater. Interfaces*, 2016, **8**, 3208–3214.
47 J. Zhang, K. A. S. Usman, M. A. N. Judicpa, D. Hegh, P. A. Lynch and J. M. Razal, *Small Methods*, 2023, **7**, 2201527.
48 W. Hou, Y. Sun, Y. Zhang, T. Wang, L. Wu, Y. Du and W. Zhong, *J. Alloys Compd.*, 2021, **859**, 157797.
49 T. Wang, K. Yao, Y. Hua, E. G. Shankar, R. Shanthappa and J. S. Yu, *Chem. Eng. J.*, 2023, **457**, 141363.
50 P. P. Waghmaitar, S. B. Alex, L. Vazhayal, S. Kad, R. R. Urkude, B. Ghosh and S. K. Haram, *ACS Appl. Energy Mater.*, 2025, **8**, 14519–14529.
51 B. Hu, Y. Xie, Y. Yang, J. Meng, J. Cai, C. Chen, D. Yu and X. Zhou, *Dalton Trans.*, 2023, **52**, 12002–12009.
52 Z. Q. Liu, K. Xiao, Q. Z. Xu, N. Li, Y. Z. Su, H. J. Wang and S. Chen, *RSC Adv.*, 2013, **3**, 4372–4380.
53 M. X. Jin, Y. L. Pu, Z. J. Wang, Z. Zhang, L. Zhang, A. J. Wang and J. J. Feng, *ACS Appl. Energy Mater.*, 2019, **2**, 4188–4194.
54 A. P. Grosvenor, M. C. Biesinger, R. S. C. Smart and N. S. McIntyre, *Surf. Sci.*, 2006, **600**, 1771–1779.

55 B. Laïk, M. Richet, N. Emery, S. Bach, L. Perrière, Y. Cotrebil, V. Russier, I. Guillot and P. Dubot, *ACS Omega*, 2024, **9**, 40707–40722.
56 P. W. Anderson, *Phys. Rev.*, 1950, **79**, 350–355.
57 J. B. Goodenough, *Phys. Rev.*, 1955, **100**, 564–573.
58 D. Goldfarb and S. Stoll, *EPR Spectroscopy: Fundamentals and Methods*, Wiley, 2018.
59 C. P. Poole Jr and H. A. Farach, *Theory of Magnetic Resonance*, Wiley, 2nd edn, 1987.
60 S. Li, L. Shi, Y. Guo, J. Wang, D. Liu and S. Zhao, *Chem. Sci.*, 2024, **15**, 11188–11228.
61 Y. Wang, J. Qian, J. Zheng, J. Li, A. Sun, J. Xing, L. Liu and Y. Zheng, *J. Alloys Compd.*, 2024, **1004**, 175821.
62 Y. Zheng, S. Chen, X. Yu, K. Li, X. Ni and L. Ye, *Appl. Surf. Sci.*, 2022, **598**, 153786.
63 J. Xu, Z. Zhou, T. Yang, X. Liu, G. Tang, H. Wu, D. Zhang, Y. Su, Z. Wu, Z. Pei and W. Yang, *Adv. Mater.*, 2025, **37**, e12724.
64 X. Liu, F. Zhan, D. Li and M. Xue, *Int. J. Hydrogen Energy*, 2020, **45**, 28836–28846.
65 C. Xie, W. Chen, S. Du, D. Yan, Y. Zhang, J. Chen, B. Liu and S. Wang, *Nano Energy*, 2020, **71**, 104653.
66 M. E. G. Lyons and M. P. Brandon, *J. Electroanal. Chem.*, 2009, **631**, 62–70.
67 A. C. Lazanas and M. I. Prodromidis, *ACS Meas. Sci. Au*, 2023, **3**, 162–193.
68 X. Zou, Q. Lu, J. Wu, K. Zhang, M. Tang, B. Wu, S. She, X. Zhang, Z. Shao and L. An, *Adv. Funct. Mater.*, 2024, **34**, 1–11.
69 S. Yadav and N. Kurra, *Energy Storage Mater.*, 2024, **65**, 103094.
70 S. F. Hung, Y. Y. Hsu, C. J. Chang, C. S. Hsu, N. T. Suen, T. S. Chan and H. M. Chen, *Adv. Energy Mater.*, 2018, **8**, 1–11.
71 L. Zhuang, Y. Jia, H. Liu, X. Wang, R. K. Hocking, H. Liu, J. Chen, L. Ge, L. Zhang, M. Li, C. L. Dong, Y. C. Huang, S. Shen, D. Yang, Z. Zhu and X. Yao, *Adv. Mater.*, 2019, **31**, 1805581.
72 F. T. Haase, A. Bergmann, T. E. Jones, J. Timoshenko, A. Herzog, H. S. Jeon, C. Rettenmaier and B. R. Cuenya, *Nat. Energy*, 2022, **7**, 765–773.
73 J. Huang, A. H. Clark, N. Hales, K. Crossley, J. Guehl, R. Skoupy, T. J. Schmidt and E. Fabbri, *Nat. Chem.*, 2025, **17**, 856–864.
74 J. Ma, Q. Wu, W. Zhang, Y. Li, Y. Lu, B. Liu, F. Yang and Y. Song, *Electrochim. Acta*, 2022, **432**, 141224.
75 Y. Bai, Y. Wu, X. Zhou, Y. Ye, K. Nie, J. Wang, M. Xie, Z. Zhang, Z. Liu, T. Cheng and C. Gao, *Nat. Commun.*, 2022, **13**, 6094.
76 S. Liu, B. Zhang, Y. Cao, H. Wang, Y. Zhang, S. Zhang, Y. Li, H. Gong, S. Liu, Z. Yang and J. Sun, *ACS Energy Lett.*, 2023, **8**, 159–168.
77 J. K. Nørskov, J. Rossmeisl, A. Logadottir, L. Lindqvist, J. R. Kitchin, T. Bligaard and H. Jónsson, *J. Phys. Chem. B*, 2004, **108**, 17886–17892.
78 M. Li, S. Zhou and M. Xu, *Chem. Eng. J.*, 2017, **328**, 106–116.
79 B. L. Lai, Z. H. Xiao, P. Y. Jiang, Y. Xie, N. Li and Z. Q. Liu, *ChemElectroChem*, 2022, **9**, e202101699.
80 H. Zhu, Z. Zhang, Y. Zhou, X. Jiang, F. Cai, Y. Bai and H. Ning, *J. Water Process Eng.*, 2022, **45**, 102471.
81 J. Liu, C. Chu, L. Wei, J. Feng and J. Shen, *Biosens. Bioelectron.*, 2023, **222**, 114926.

